Simulation of turbulent horizontal oil-water core-annular flow with a low-Reynolds number k–ε model

Li, Haoyu; Pourquie, M. J.B.M.; Ooms, G.; Henkes, R. A.W.M.

DOI
10.1016/j.ijmultiphaseflow.2021.103744

Publication date
2021

Document Version
Final published version

Published in
International Journal of Multiphase Flow

International Journal of Multiphase Flow 142 (2021) 103744

Contents lists available at ScienceDirect

International Journal of Multiphase Flow

journal homepage: www.elsevier.com/locate/ijmulflow

Simulation of turbulent horizontal oil-water core-annular flow with a low-Reynolds number k–ε model

Haoyu Li *, M.J.B.M. Pourquie, G. Ooms, R.A.W.M. Henkes

J.M. Burgerscentrum, Delft University of Technology, Faculty of Mechanical Engineering, Laboratory for Aero- & Hydrodynamics, Mekelweg 2, 2628 CD Delft, The Netherlands

ARTICLE INFO

Keywords:
Core-annular flow
Levitation mechanism
Interfacial waves

ABSTRACT

1D, 2D and 3D numerical simulations were carried out with the Reynolds-Averaged Navier-Stokes equations (RANS) for horizontal oil-water core-annular flow in which the oil core stays laminar while the water layer is turbulent. The turbulence is described with the Launder-Sharma low-Reynolds number $k-\epsilon$ model. The simulation results are compared with experiments carried out in our lab in a 21 mm diameter pipe using oil and water with a viscosity ratio of 1150 and a density ratio of 0.91. The 1D results represent perfect turbulent CAF (i.e. no gravity, no interfacial waves), the 2D results represent axi-symmetric CAF (i.e. no gravity, with interfacial waves), and the 3D results represent eccentric CAF (i.e. with gravity, with interfacial waves). The simulation results typically show a turbulent water annulus in which the structure of the (high-Reynolds number) inertial sublayer can be recognized. The pressure drop reduction factor (which is the ratio between the pressure drop for CAF and the pressure drop for single phase viscous oil flow) for the 2D and 3D results is about the same, but its value is about 35% higher than in the experiment. The hold-up ratio in the 3D model is close to the experimental value, but the 2D prediction is slightly lower. The eccentricity predicted by the 3D simulations is much higher than in the experiment. Most likely, the observed differences between the simulations and the experiments are due to limitations of using a low-Reynolds number $k-\epsilon$ model. In particular the water layer at the top in the 3D results shows a relaminarization, which might be absent in the experiment.

1. Introduction

Oil-water core-annular flow (CAF) is a typical two-phase flow pattern in a pipe, in which there is a viscous oil core surrounded by a water annulus. The thin water annulus lubricates the pipe wall, which significantly decreases the pressure drop compared to single phase viscous oil transport. For example, this kind of flow pattern is applicable in transporting highly viscous oil in the petroleum industry. In addition to its application opportunities, core-annular flow is also of great interest from a more fundamental fluid mechanics perspective.

At relatively low flow rates, both the oil core and the water annulus will be laminar. But if the flow velocities become higher, the water annulus will become turbulent. Further increase of the flow rates will give dispersion of the oil as droplets in the water, with oil fouling of the pipe wall. At low flow rates in a horizontal pipe a stratified water-oil layer will be found. This core-annular flow is only a single flow regime within the flow pattern map. The occurrence of core-annular flow (and the characteristics of the core-annular flow) depend on a range of parameters, such as: the pipe inclination, the pipe diameter, the total flow rate, the fraction of water in the total flow rate (which is the watercut), the ratio of the oil viscosity and the water viscosity, the ratio of the oil density and the water density, and the interfacial tension between the oil and the water.

For given conditions, the key parameters are the pressure gradient and the water holdup fraction. Core-annular flow is characterized by waves at the interface. The presence of this interface will cause a stress in flow direction between the oil core and the water annulus. The resulting interfacial force will consist of a contribution due to the shear stress and due to form drag. The latter is the resultant of the pressure working on the wavy interface in main flow direction. This interfacial stress will give water accumulation, which means that the water holdup fraction is higher than the watercut.

Over the past decades much research has been devoted to CAF, for vertical upflow and, albeit to a lesser extent, also for horizontal flow. This includes the pioneering work of Daniel Joseph and his team; an overview is given by Joseph et al. (1997). Huang and Joseph (1995),

* Corresponding author.
E-mail address: H.li-6@tudelft.nl (H. Li).

https://doi.org/10.1016/j.ijmultiphaseflow.2021.103744
Received 28 January 2021; Received in revised form 24 May 2021; Accepted 1 July 2021
Available online 6 July 2021

Preziosi et al. (1989), and Chen et al. (1990) studied the stability of core-annular flow, showing bamboo-shaped waves in both their experimental and numerical results. Li and Renardy (1999) carried out a numerical study of vertical CAF with the linear and non-linear stability of interfacial waves. Recently, Song et al. (2019) determined the different linear and nonlinear instability mechanisms for a laminar vertical CAF by using a phase-field method to capture the deformation of the oil-water interface. For a horizontal pipe, as gravity is now acting perpendicular to the pipe axis, and as the density of the oil core is smaller than the density of the water annulus, eccentric CAF will occur. The presence of waves at the oil-water interface is crucial for the levitation mechanism, i.e. this will generate a downward force to counterbalance the upward buoyancy force. Ooms et al. (1984) developed a lubrication film model by assuming a sawtooth-shaped wave at the interface. Ooms et al. (2007, 2012, 2013) performed a numerical study in the laminar case for eccentric horizontal CAF with a low Reynolds number in the annulus layer. Based on lab experiments in vertical and horizontal pipes for CAF at various conditions (flow rates, watercut, oil/water viscosities and densities) various correlations were derived for the pressure drop and the holdup. See for example the work by Arney et al. (1993), who provided an empirical correlation for the holdup and who used a concentric cylindrical CAF model to find a correlation for the pressure drop that only depends on a single Reynolds number. An overview of available correlations is given by Ghosh et al. (2009). Also Bannwart (2001) gave an overview of modelling for CAF, and he concludes that "pressure drop in horizontal core–annular flow should take into account the turbulence in the annulus and waviness of the interface; these aspects lead to a correlation very different from the PCAF model (laminar–laminar flow with a smooth interface)".

To illustrate the rich physics of the flow of two immiscible liquids, reference is made to the experimental study by Hasson et al. (1970). They injected two liquids with almost the same viscosity, but with a slightly different density, in a 12.6 mm diameter horizontal pipe. Initially the lighter liquid was flowing in the core and the heavier liquid was flowing in an annulus, giving CAF with travelling interfacial waves. A flow visualization was made to assess whether the CAF could be maintained over the length of the pipeline. One instability mechanism (Rayleigh instability), being due to the interplay of interfacial tension and inertia, gave a growth of the interfacial wave into the core, such that the core structure was broken leading to slug flow. The CAF could also end due to the ascend of the lighter liquid core towards the pipe top, leading to the disruption of the annulus film. If only an incidental touch of the top wall by the lighter liquid did occur, the breakage of the annulus was also dependent on the wettability properties of the liquids. Quite recently, Roccon et al. (2019, 2021) carried out Direct Numerical Simulations (DNS) for two immiscible liquids in a channel. Another liquid type with a small flow rate was added to the bulk flow of the original type; the additional liquid amount was meant to give a lubrication effect with pressure reduction. Initially the two viscosities were taken equal. As the two liquids are immiscible (as indicated by the finite interfacial tension) an interface will be formed that leads to the replacement of the turbulent flow along the lubricated pipe wall by laminar flow, which in turn gives a lower pressure drop as compared to the case with single phase flow. Decreasing the viscosity of the lubricated fluid by a factor 4 will keep the flow in a turbulent state, but this still leads to a small pressure reduction as the presence of the interface mitigates the size of the eddies in the lubrication layer (as compared again to the case with single phase flow). In contrast to the work by Roccon et al., in our study, a high viscosity core fluid will be considered, but the relaminarization phenomenon (depending on the local shear-based Reynolds number) will turn out to remain very relevant.

The present study extends the conditions for horizontal CAF (with a highly viscous oil core) to a higher flow rate (or larger pressure drop), with a higher Reynolds number, in which a turbulent (instead of laminar) water flow in the annulus is found (while the viscous oil core is still laminar). Both lab experiments and numerical simulations will be presented. The numerical simulations are based on solving the unsteady Reynolds-Averaged Navier-Stokes (RANS) equations with the Launder & Sharma low-Reynolds number $k-\epsilon$ model. The idea is that the wave formation at the interface is still captured by the unsteady terms with the RANS, but that the high-frequency, small scale turbulent structures are represented by the Reynolds stresses, which in turn are described by closure relations using the $k-\epsilon$ model. The low-Reynolds number $k-\epsilon$ model is expected to work well for the turbulent boundary layer (within the water annulus) along the pipe wall, but may show shortcomings in describing the recirculation zones that will be found in the interfacial wave troughs (as experienced by an observer travelling with the waves).

A few studies exist in which turbulence modelling has been used for CAF. Huang et al. (1994) have applied the Launder & Spalding low-Reynolds number $k-\epsilon$ model to the eccentric water annulus in horizontal core-annular flow. The lift mechanism, which determines where the levitated core is located, is associated with interface deformations, but this has been neglected in that study. Instead, the eccentricity is prescribed in their model, and the oil core is represented by a solid cylinder without waves. Therefore only the single-phase, steady, 2D RANS equations had to be solved for the eccentric water annulus. Ko et al. (2002) have used the Shear Stress Transport (SST) $k-\omega$ model in their steady, single-phase RANS simulations for the turbulent water annulus in concentric, axisymmetric CAF in a horizontal pipe. The axi-symmetric assumption means that gravity effects are not included. The steady equations are solved, in which the pipe wall has been given a velocity opposite to the wave velocity. The oil core is assumed to be solid. The wave pattern at the interface is obtained by the applying the Young-Laplace pressure jump that results from the interfacial tension at the curved interface. Shi et al. (2017a, 2017b) and Archibong-Eso et al. (2017) have used the Shear Stress Transport (SST) $k-\omega$ model in their 3D RANS simulations in the Fluent CFD package for horizontal water-oil flow. The focus in their studies was on obtaining an overview of the different flow regimes that can occur (i.e. CAF, water droplets in oil, oil droplets in water, oil plugs in water), with the corresponding pressure drop and water holdup fraction. The details of the waves and turbulence were not reported. Quite recently, Kim and Choi (2018) have carried out Direct Numerical Simulations (DNS) for vertical CAF with a laminar (very viscous) oil core and with a turbulent water annulus. Obviously, such simulations require a very fine numerical grid, and small numerical time steps, but have the advantage that the waves and turbulence are fully resolved. A method in between DNS and RANS is Large-Eddy Simulations (LES), but we are not aware of any examples where LES has been applied to CAF.

The simulation set up in the present study is based on CAF experiments that were recently carried out in our lab by Van Duin et al. (2019) and that have been extended to obtain interface data that will be used for comparison. The pipe is horizontal with a 21 mm diameter. The viscous oil core is laminar and the water annulus is turbulent. The viscosity ratio between the oil and water is 1150, and the density ratio is 0.91. Simulations are carried out for cases both without gravity (using 1D and 2D formulations) and with gravity (using a 3D formulation). In particular the velocity profile and the turbulent structure in the water annulus are studied. Furthermore, the eccentricity and the levitation mechanism of the oil core and the related interfacial waves are examined. A force balance is performed on the oil core and the levitation force is split into the reduced pressure force and the viscous force.

2. Experimental and numerical method

2.1. Lab experiments

Flow measurements (pressure drop and flow visualization) were carried out in the horizontal core-annular flow loop (with 21 mm internal diameter) of our lab. The same loop was used in a previous study (Van Duin et al., 2019), but for the present study additional measurements for the water annulus thickness were obtained. The flow loop is

approximately 7.5 m long and is partly made of PVC. The measurement section is 3 m long and is made of plexiglas (PMMA) to give good optical access. Near the end of this measurement pipe there are two points (spaced 1 m apart) to measure the pressure drop. Between these two points is the optical box, made of PMMA and filled with water, where the visualisation takes place. Through using mirrors, a high speed camera can simultaneously record the water annulus at the top, bottom, left and right sides of the pipe.

Upstream of the inlet of the pipe there is a 60 litre oil tank. In the tank there is a copper coil for heating, which allows to change the oil viscosity. Water is taken from the tap. A pump is used to circulate the flow. The oil flow rate is measured through the calibrated pump frequency and the water flow rate is measured through a Biotech turbine meter. At the inlet of the pipe there is a divider, in which the oil is added through a concentric pipe and water is added in through an annulus, to create core-annular flow. At the end of the flow loop there is a three way valve that will either send the content of the flow loop to the rinsing tank or to the separation barrel. There also is an approximately 200 litre barrel where the oil-water mixture from the experiment is separated. Inside the barrel there is a floater that is attached to a small electrical gear pump, which pumps the oil back to the oil tank. At the bottom there is a drain valve which is used to dispose the excess water in the tank after the oil has been pumped back to the tank.

The main purpose of this experiment is to measure the water film thickness (in space and time). The camera used for this visualisation is a Phantom Vision VEO 640L. A LED panel is placed behind the optical box to illuminate the measurement section so that clear images are produced. To mitigate the amount of optical distortion, an optical box is attached to the measurement section. Since the thickness of the water film is small (order of a mm only), it is important to correct for any remaining distortion of the image. Thereto the experiment was calibrated by using a test pipe section with a calibration grid. In addition this was also verified by reconstructing the light paths with a ray-tracing calculation method. An example of the flow visualization and the wall correction is given in Fig. 1.

2.2. Governing equations

The mass and momentum conservation equations for an incompressible, isothermal fluid are (in cartesian coordinates):

$$\frac{\partial u_i}{\partial x_i} = 0 \tag{1}$$

$$\frac{\partial \rho u_i}{\partial t} + \rho u_j \frac{\partial u_i}{\partial x_j} = \frac{\partial}{\partial x_j}\left(\rho(\nu + \nu_t)\left(\frac{\partial u_i}{\partial x_j} + \frac{\partial u_j}{\partial x_i}\right)\right) - \frac{\partial p}{\partial x_i} + \rho g_i + F_{\sigma,i} \tag{2}$$

These are the Reynolds-Averaged Navier-Stokes Equations (RANS). Here u_i is the velocity, ρ and μ are the fluid density and viscosity, $g_i$is the gravitational acceleration, p is the pressure and $F_{\sigma,i}$ is the interfacial tension force. For the pipe flow, we will use $x_1 = x$ for the coordinate along the pipe axis, $x_2 = y$ for the vertical coordinate, and $x_3 = z$ for the pipe width coordinate; the velocity components are u, v, and w, in the directions x, y, and z, respectively. The gravity components are: g_1=g_3=0, and $g_2 = -g$, where g is the gravitational acceleration.

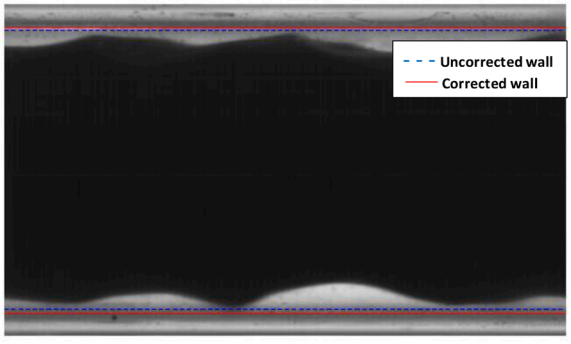

Fig. 1. Snapshot of the flow visualization in the lab experiment, showing the wave structure (flow is from left to right).

The turbulent viscosity is modelled with the low-Reynolds number $k-\epsilon$ model of Launder and Sharma (1974), which reads as follows:

$$\nu_t = C_\mu f_\mu \frac{k^2}{\widetilde{\varepsilon}} \tag{3}$$

$$\frac{\partial k}{\partial t} + u_j \frac{\partial k}{\partial x_j} = \frac{\partial}{\partial x_j}\left(\nu + \frac{\nu_t}{\sigma_k}\right)\frac{\partial k}{\partial x_j} + \nu_t\left(\frac{\partial u_j}{\partial x_j}\right)^2 - \widetilde{\varepsilon} - D \tag{4}$$

$$\frac{\partial \widetilde{\varepsilon}}{\partial t} + u_j \frac{\partial \widetilde{\varepsilon}}{\partial x_j} = \frac{\partial}{\partial x_j}\left(\nu + \frac{\nu_t}{\sigma_\varepsilon}\right)\frac{\partial \widetilde{\varepsilon}}{\partial x_j} + C_1 f_1 \frac{\widetilde{\varepsilon}}{k}\nu_t\left(\frac{\partial u_j}{\partial x_j}\right)^2 - C_2 f_2 \frac{\widetilde{\varepsilon}^2}{k} + E \tag{5}$$

With $D = 2\nu\frac{\partial\sqrt{k}}{\partial x_j}\frac{\partial\sqrt{k}}{\partial x_j}$ and $E = 2\nu\nu_t\left(\frac{\partial u_j}{\partial x_j}\right)^2$. The turbulent energy dissipation rate is $\varepsilon = \widetilde{\varepsilon} + D$. Furthermore, $C_\mu = 0.09$, C_1=1.44, C_2=1.92, σ_k=1.0, σ_ε=1.3, $f_\mu = \exp\left(\frac{-3.4}{\left(1+\frac{Re_t}{50}\right)^2}\right)$, f_1=1, $f_2 = 1 - 0.3\exp(-Re_t^2)$, $Re_t = \frac{k^2}{\varepsilon\nu}$. The boundary conditions at the wall are: k=0 and $\widetilde{\varepsilon} = 0$.

Quite a number of low-Reynolds number $k-\epsilon$ formulations are available in the literature. A large advantage of the Launder-Sharma one is that the low-Reynolds number terms do not include the explicit distance to the closest wall. Instead the parameter Re_t is used to incorporate the effect of turbulence damping when a wall is approached. In the same way, the model will incorporate the possible damping of turbulence when the oil-water interface is approached in core-annular flow. The low-Reynolds number $k-\epsilon$ model is used everywhere in the domain, also in the laminar oil core. Because of the presence of the low-Reynolds number terms the model automatically relaminarizes in the viscous oil core (i.e. it gives zero turbulent viscosity).

2.3. Numerical method

We used the open-source package OpenFOAM to solve the RANS equations, applying the CLVOF method for the interface capturing. The CLSVOF solver, which was developed by Yamamoto et al. (2017), is based on the interFoam Volume of Fluid (VOF) solver in OpenFOAM. The level set function is used to calculate the interfacial tension force. Starting from the VOF method, the oil volume fraction α is introduced to distinguish between the two fluid phases: $\alpha = 0$ is the oil phase, $\alpha = 1$ is the water phase, and $0 < \alpha < 1$ denotes the oil-water interface. Then the fluid density and viscosity in the equations are:

$$\rho = (1-\alpha)\rho_o + \alpha\rho_w \tag{6}$$

$$\mu = (1-\alpha)\mu_o + \alpha\mu_w \tag{7}$$

The subscript "o" refers to oil, and the subscript "w" refers to water. α is calculated from the following advection equation:

$$\frac{\partial \alpha}{\partial t} + \nabla\cdot(\alpha\vec{u}) + \nabla\cdot\left((1-\alpha)\alpha\vec{u}_r\right) = 0 \tag{8}$$

The third term on the left-hand side is the compressive term (with the divergence of compressive flux); here $\vec{u}_r = \vec{u}_w - \vec{u}_o$. The term is meant to control the sharpness of interface.

The level set function Φ is defined as the distance from the interface, where the interface is the isoline with $\Phi = 0$. The initial value of the level set function Φ_o is obtained from the initialized volume-of-fluid field, where the interface is defined at $\alpha = 0.5$:

$$\Phi_0 = (2\alpha - 1)\Gamma \tag{9}$$

$$\Gamma = 0.75\Delta X \tag{10}$$

Here ΔX is the minimum mesh size near the interface. Thereafter the re-initialization equation is solved to turn the initial level set function into the distance from the interface:

$$\frac{\partial \Phi}{\partial \tau} = \text{sign}(\Phi_0)(1 - |\nabla \Phi|) \tag{11}$$

Here $\tau = 0.1\Delta X$ is the iteration time step of Φ and the sign function denotes:

$$\text{sign}(\Phi) = \begin{cases} 1 \ \Phi > 0, \ \text{water} \\ 0 \ \Phi = 0, \ \text{interface} \\ -1 \ \Phi < 0, \ \text{oil} \end{cases} \tag{12}$$

Then the interface tension force is calculated as:

$$\vec{F}_\sigma = \sigma \kappa(\Phi) \delta_\Phi \nabla(\Phi) \tag{13}$$

Here σ is the interface tension and δ_Φ is the smoothed delta function:

$$\delta_\Phi = \begin{cases} \frac{1}{2\gamma}\left(1 + \cos\left(\frac{\pi \Phi}{\gamma}\right)\right) \ \text{for} \ |\Phi| < \varepsilon \\ \text{elsewhere} \end{cases} \tag{14}$$

The quantity γ is the interface thickness coefficient (see Yamamoto et al., 2017) and $\kappa(\Phi)$is the interface curvature:

$$\kappa(\Phi) = \nabla \cdot \vec{n}_c \tag{15}$$

$$\vec{n}_c = \frac{(\nabla \Phi)_f}{|(\nabla \Phi)_f|} \tag{16}$$

Here $\vec{n}_c$ is the surface unit normal vector. The contact angle θ between the interface and the pipe wall is defined as:

$$\cos(\theta) = \vec{n}_c \cdot \vec{n}_w \tag{17}$$

With $\vec{n}_w$ being the unit normal vector at the wall. The contact angle is set to 90^o in our simulations. This means that both the level set function Φ and the volume fraction of the fluid α satisfy the zero gradient condition at the pipe wall boundary.

A perfect (laminar) core-annular flow (which means that the oil core is cylindrical and concentric) is set as an initial condition. An analytical (laminar) velocity profile is set for the whole flow domain:

$$u^*(r^*) = \begin{cases} \left(a^2 - r^{*2}\right)/A \ 1 \le r^* \le a \\ 1 - m r^{*2}/A \ r^* < 1 \end{cases} \tag{18}$$

$$A = m + a^2 + 1$$

Where $r^* = r/R_c$ is the dimensionless distance to the pipe centre, R_c is the oil core radius, $a = R/R_c$ is the ratio of the pipe radius and the oil core radius, $m = \mu_w/\mu_o$ is the ratio of the water viscosity and the oil viscosity. $u^* = u/u_c$ is the dimensionless velocity in the main flow direction, where u_c is the centreline velocity. Note that this velocity profile is only used to start the simulation. Of interest is the oscillating solution obtained after some time, which is (supposed to be) independent of the start condition.

A pressure drop in the flow direction is added as an extra force term to the right-hand side of Eq. (2), with periodic boundary conditions on the left and right side of the pipe. The velocity profile will then develop over time under this pressure drop in the transient simulation until a stable state (with an eccentric oil core) is obtained. Therefore, the pressure that remains in the equations is periodic with respect to the left and right side of the computational pipe section.

A second-order backward implicit time discretization scheme is applied, with a very small time step (small Courant number). This gives a very accurate time integration. We use a second-order scheme for the advection terms in the momentum equations and in the interface equation (as used in the level set method), but a first-order upwind scheme for the advection in the equations for the turbulence quantities k and ε; trying a second-order scheme for the latter gave numerical instabilities. Through successive mesh refinement, however, we have demonstrated (see the details later) that the simulation results are accurate (and not suffering from large numerical diffusion).

In all the simulations, periodic boundary conditions are applied on the left and right side of the pipe, which restricts the wavelengths in the axial direction to twice the domain length divided by an integer value. At the pipe wall, the no-slip condition is imposed. We have used the symmetric PBiCG solver for the velocity and for the turbulent quantities, the GAMG solver for the pressure, and the PIMPLE solver for the velocity-pressure coupling.

2.4. Considered base conditions

The simulation conditions were the same as in the lab experiment. The pipe radius is R=0.0105 m (pipe diameter is 21 mm). The length of the pipe section is set to 0.0256 m (25.6 mm), which is twice the most dominant wavelength, as estimated from a linear instability analysis (albeit for laminar flow) by Beerens et al. (2014). The fluid properties are set as follows: the oil and water kinematic viscosity are $\nu_o = 7.73 \times 10^{-4}$ m^2/s and $\nu_w = 6.7 \times 10^{-7}$ m^2/s, the oil and water densities are $\rho_o = 902$ kg/m^3 and $\rho_w = 993$ kg/m^3, and the interfacial tension between oil and water is $\sigma = 0.016$ N/m (Shell Morlina S2 B 680 at 40 °C was used in the experiments). Note that the ratio between the kinematic viscosities of oil and water is 1150, and the density ratio between the oil and water is $\rho_o/\rho_w = 0.91$. The Reynolds number in wall units, i.e. $Re_\tau = d^+ = u_\tau d/\nu_w$, is about 150 (here u_τ is the wall shear stress velocity and d is the average thickness of the water annulus). This is above the minimum value of about 90 which is needed to sustain turbulence in single phase channel flow (where d is half the channel width); this criterion was derived by Jimenez and Moin (1991), who applied DNS to channel flow. The occurrence of turbulence in the water annulus is confirmed in the present simulations, which show an inertial sublayer with a maximum turbulent viscosity (ν_t/ν_w) of about 20.

2.5. Key parameters

Four important parameters are: the total flow rate, the pressure drop, the watercut, and the water hold-up fraction. When two parameters are set as input (e.g. the total flow rate and the watercut in the experiments), the other two will follow as output.

The watercut is defined as the ratio of the water volumetric flow rate and the total volumetric flowrate:

$$WC = Q_w/(Q_o + Q_w) \tag{19}$$

where Q denotes the volumetric flow rate. The water hold-up fraction is defined as the ratio of the in-situ water volume in the pipe and the total volume of oil and water:

$$\alpha_w = \frac{V_w}{V_w + V_o} \tag{20}$$

A related parameter is the so-called hold-up ratio h, which is defined as:

$$h = \frac{Q_o/Q_w}{V_o/V_w} \tag{21}$$

This can also be rewritten as $h = 1 + u_r/u_w$. Here the velocity difference $u_r = u_o - u_w$, is the apparent (average) slip velocity between the oil core (having a bulk velocity u_o) and the water annulus (having a bulk velocity u_w). Note that h=1 if there is no slip between the bulk oil and water velocities. The hold-up ratio thus is a measure of the apparent slip between the oil core and the water annulus.

2.6. Verification of the simulations

To verify the implementation of the Launder& Sharma low-Reynolds number $k-\epsilon$ model in the OpenFOAM CFD package, we have coded the same model in Matlab, though using the 1D equations. 1D means that perfect core-annular flow is considered, though allowing for a turbulent water annulus. "Perfect" means that the oil core is concentric (i.e. no gravity in a horizontal pipe) and that there are no waves on the water-oil interface. The 1D model also allowed to determine the required grid resolution close to the wall for the accurate representation of the turbulent profiles. Similar 1D simulations were carried out with OpenFOAM. There was excellent agreement between the results obtained with the two simulation models.

To verify the numerical accuracy of the mesh resolution in OpenFOAM, first the 2D axi-symmetric case is studied, because such a simulation requires far less computer time than a full 3D simulation. We imposed a constant total flow rate of 4.3×10^{-4} m^3/s (which is the value applied in the lab experiment). To obtain a watercut of (about) 20% (being the same as in the experiment condition), the water hold-up fraction in the simulation had to be set to 0.257. Therefore in these simulations the total flow rate and the water hold-up fraction were used as boundary conditions, whereas the pressure drop and the watercut are obtained as output values.

For the mesh refinement, the following stretch function is used in the radial direction:

$$\frac{y_j}{y_{jmax}} = 1 + \frac{\tanh[\alpha_1(j/jmax - 1)/2]}{\tanh(\alpha_1/2)}, j = 0, 1, ..., jmax \tag{22}$$

Where *jmax* is the total number of mesh points and y_{jmax} is the coordinate of the j^{th} node. A proper value of α_1 is used to ensure that there are several grid points in the viscous sublayer along the pipe wall. The stretch function will make the mesh smooth (which improves the numerical accuracy and increases the simulation speed). The coefficient α_1 is found from the expression $\alpha_2 = \alpha_1/\sinh(\alpha_1)$, in which α_2 is close to zero. In the present simulations we took $\alpha_2 = 0.26$, in order the make sure that some grid points are located in the viscous sublayer along the pipe wall. A uniform mesh is used in the axial direction. In the 3D case, also a uniform mesh is used in the circumferential direction.

Table 1 summarizes the values of key quantities at successively refined meshes in the 2D simulations (100 × 100, 200 × 200, and 400 × 400). The quantities shown in the table were obtained by analysing the temporal results at a fixed streamwise location in the simulated pipe section. It turns out that the wave velocity is practically independent of the local water annulus thickness (or the local wave height). This means that the temporal wave evolution can be converted to the spatial wave propagation through using this constant wave velocity (i.e. the Taylor hypothesis applies). The simulated section length of 25.6 mm shows precisely 2 waves; the wave length thus is 12.8 mm. The wave amplitude is defined as

$$A = \sqrt{2\overline{(\delta - \bar{\delta})^2}} \tag{23}$$

Here an overbar denotes the time-averaged value (as determined at a fixed *x*-location in the pipe); δ is the thickness of the water annulus. The amplitude is defined such that it gives the usual value of the amplitude for the case that the wave is a pure sinus (where the amplitude is half the difference between the maximum and the minimum value). Note that definition (23) for the amplitude is also meaningful for an irregular time dependence of the water annulus thickness (i.e. without a single frequency). Fig. 2 gives an example of the simulated wavy interface.

Mesh refinement does not yet show the full asymptotic decay of the numerical error, but the differences between the various meshes are quite small. This is shown for the oscillating thickness of the water annulus in Fig. 3. The table also confirms that some grid points are located in the viscous sublayer along the pipe wall (y+<5). This is important because here the turbulence is damped by the low-Reynolds number terms in the $k-\epsilon$ model. Having sufficient grid points here is essential for obtaining an accurate numerical value for the wall shear stress, and thus for the pressure drop. As shown in the table, the pressure drop still shows some mesh dependence (from 814 Pa/m on the 100 × 100 mesh to 748 Pa/m for the 400 × 400 mesh). To verify the importance of having sufficient grid points very close to the wall, the simulation with 100 × 100 points was repeated with a different value of the stretching parameter in Eq. (22), giving the first inner grid point at y^+=0.6 instead of 3; this indeed improves the prediction of the pressure drop from 814 to 746 Pa/m (with the latter value being close to 748 Pa/m found on the very fine 400 × 400 mesh). There are also a significant number of grid points through the wavy interface. In the 2D simulations, considering the number of points in radial direction covering the wave between its crest and trough, we have about 25 points for the 100 × 100 mesh, 50 points for the 200 × 200 mesh, and 100 points for the 400 × 400 mesh.

The applied mesh in the 3D simulations is as follows. Near the origin we use a pentagon area, which is covered with a structured O-grid. This area is part of the laminar oil core. Around this area there is a cylindrical area up to the pipe wall that applies an axi-symmetric grid. This covers the outer part of the oil core, the wavy oil-water interface and the water annulus. Here we use an axi-symmetric grid with a uniform distribution in azimuthal direction. The mesh stretching function in radial direction is the same as used in the 2D axisymmetric simulations. Based on the 2D mesh verification results, the mesh resolutions of 100 × 200 × 80 points and 100 × 200 × 160 points were used in axial, radial, and the circumferential direction, respectively, in the 3D simulations. In the verification of the 3D results the imposed pressure drop was 725 Pa/m and the imposed water holdup fraction was 0.257. It is found that the results, such as the total flow rate, are not very sensitive to the resolution in the circumferential direction; the total flow rate is 4.8×10^{-4} m^3/s with 80 points in circumferential direction and 4.7×10^{-4} m^3/s with 160 points in circumferential direction. However, there is more dispersion of oil droplets in the water annulus with the 80 points than

Table 1
Mesh verification in the 2D case.

Quantity	Unit	100 × 100	200 × 200	400 × 400
Imposed total flow rate	m^3/s	0.00043	0.00043	0.00043
Imposed water hold up fraction		0.257	0.257	0.257
Water cut	%	21.4	21.9	22.2
Pressure drop	Pa/m	814	818	748
Water layer thickness	mm	1.53	1.51	1.49
Wave amplitude	mm	0.60	0.71	0.73
Wave velocity	m/s	1.23	1.24	1.25
Wave frequency	Hz	96.1	96.7	97.7
Wave length	mm	12.8	12.8	12.8
Maximum ν_t/ν_w		17.2	16.9	18.8
y+ value at the first inner grid point		3	1	0.6

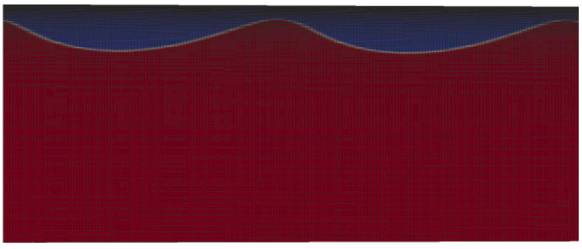

Fig. 2. Snapshot of the 2D axi-symmetric simulation showing the oil-water interface together with the 200 × 200 mesh. The travelling waves at the interface move from left to right. The water layer is shown in blue, the oil core in red, and the interface is shown as a white line.

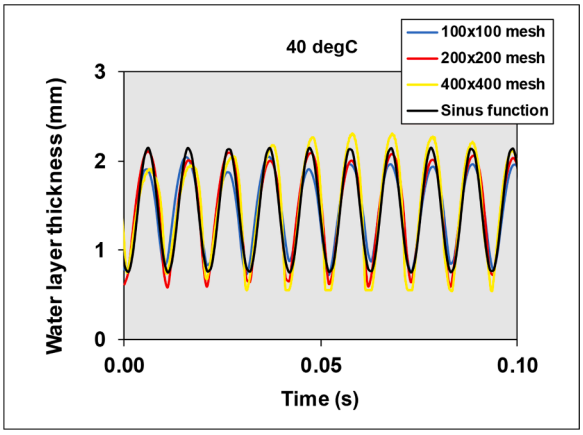

Fig. 3. Mesh dependence of the oscillating thickness of the water annulus. For comparison, also a purely sinusoidal oscillation is included.

with the 160 points. The mesh resolution with 160 points in circumferential direction is concluded to be adequate; the 3D results obtained with the 100 × 200 × 160 mesh resolution will be discussed in this paper.

3. 1D results

The base case conditions for the comparison between the simulation results and the lab experiments are the total flow rate of 0.00043 m^3/s and a watercut of 20%. The oil viscosity is $\nu_o = 7.73 \times 10^{-4}$ m^2/s (and the other oil and water properties are those specified in Section 2.4). The corresponding average velocity (or the mixture velocity, being the ratio of the total flow rate and the cross section of the pipe) is 1.24 m/s.

The 1D model (which means that there is no gravity effect and no interfacial waves) gives a pressure drop of 418 Pa/m and a water holdup fraction of 0.320 (these results are fully grid-independent). This pressure drop is significantly higher than the value of only 108 Pa/m for laminar perfect CAF, which shows the effect of turbulence in the water annulus (but the water holdup fraction for laminar flow remains about the same at 0.333). The predicted pressure drop with the turbulent water annulus is significantly lower than the experimental value of (about) 1100 Pa/m and the water holdup fraction is significantly higher than the experimental value of (about) 0.257. The difference is not surprising, as a flat interface (no waves) has been assumed in this model, being perfect turbulent CAF. However, the 1D model already gives a good impression

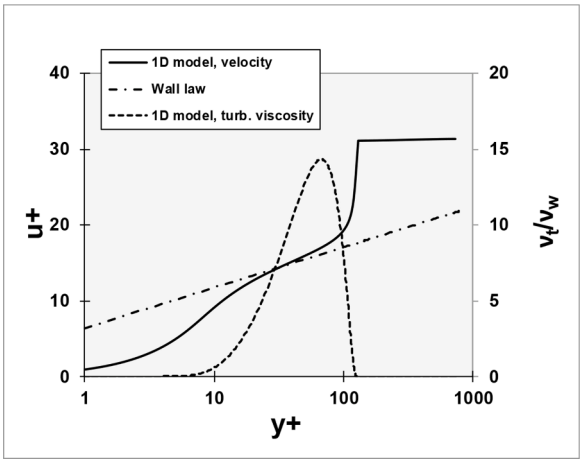

Fig. 4. 1D velocity and turbulent viscosity; total flow rate is 0.00043 m^3/s, watercut is 20% (oil viscosity is $\nu_o = 7.73 \times 10^{-4}$ m^2/s). Distance to wall is $y = R - r$.

of the turbulence in the water annulus. Thereto, Fig. 4 shows the streamwise velocity profile and the turbulent viscosity. Here the distance to the wall is y=R-r. The velocity and distance are given in the familiar "plus" units (or wall units, using the wall shear velocity and the kinematic water viscosity). The turbulent viscosity is scaled with the kinematic water viscosity. The water annulus is driven by the combined effect of the pressure gradient and the oil core movement. This gives the Couette like velocity profile, which closely follows the logarithmic law-of-the-wall in the inertial sublayer (which is between about y^+ is 10 and 100 in this simulation). Close to the interface, the water velocity shows a sharp increase to reach the oil core value.

It is convenient to use the 1D model to verify the scaling of the turbulent water annulus. The model runs very fast and fully grid-independent results can be obtained. Thereto the shear-based Reynolds number for the water layer was increased with a factor 10 and 100 with respect to the its base value; see the results in Fig. 5. As shown by Henkes (1998), the Launder & Sharma low-Reynolds number $k-\epsilon$ model will give the following asymptotic behaviour in the intertial sublayer of wall-bounded turbulent flow:

$$u^+ = \frac{1}{\kappa} ln\ y^+ + C,\ \nu_t^+ = \kappa y^+,\ k^+ = \frac{1}{\sqrt{C_\mu}},\ \varepsilon^+ = \frac{1}{\kappa y^+} \tag{24}$$

With κ =0.431, C =6.4 C_μ = 0.09 (these parameters hold for the Launder & Sharma formulation). The + superscript refers to quantities scaled with the kinematic water viscosity ν_w and with the wall shear velocity $u_\tau = \sqrt{\tau_w/\rho_w}$ (in which τ_w is the wall shear stress):

$$u^+ = u/u_\tau, \nu_t^+ = \nu_t/\nu_w,\ k^+ = k/u_\tau^2, \epsilon^+ = \tilde{\epsilon}\nu_w/u_\tau^4 \tag{25}$$

As shown in Fig. 5, an increasing Reynolds number for the water annulus gives an increasing range of y^+, which gives converge to the asymptotic wall laws specified in Eq. (24). The intertial subrange for the relatively low Reynolds number that corresponds with the experimental conditions that are the main focus of the present study is relatively small (namely from about y^+=10 to 100). But despite this, the Reynolds number is already sufficiently high to give fully turbulent flow that is close to the asymptotic law-of-the-wall behaviour. When analysing the 2D and 3D results in the subsequent sections, the wall laws will again be shown for comparison.

4. 2D results

The prescribed conditions in the 2D simulations were a total flow rate of 0.00043 m^3/s and a water holdup fraction of 0.257. This gives as output a watercut of 22% and a pressure drop of about 750 Pa/m (see Table 1). The water holdup fraction and watercut are in agreement with the experimental values (being 0.257 and 20%). The pressure drop is still significantly underpredicted (by about 30% compared to 1100 Pa/m), though this already means a large improvement compared to the 1D case. Also the 2D results for the water holdup / watercut in 2D are much better than for the 1D case. As expected, allowing for the presence of waves in the model is crucial for the prediction of the pressure drop in core annular flow.

The average oil velocity (being the ratio of oil flow rate and the oil holdup fraction) is 1.30 m/s, and the average water velocity (being the ratio of the water flow rate and the water holdup fraction) is 1.06 m/s. The mixture velocity is 1.24 m/s.

The waves in the 2D results move with a practically constant velocity of 1.24 m/s (independent of the local wave height, or of the local thickness of the water annulus); the wave velocity happens to be equal to the mixture velocity here (which is in between the average oil velocity and the average water velocity). This constant wave velocity means that an observer traveling with this wave velocity will experience a steady state flow (with the RANS approach). That flow as seen from a reference frame moving with the wave velocity is depicted in Fig. 6 for the streamlines, pressure and turbulent viscosity. When defining the waves

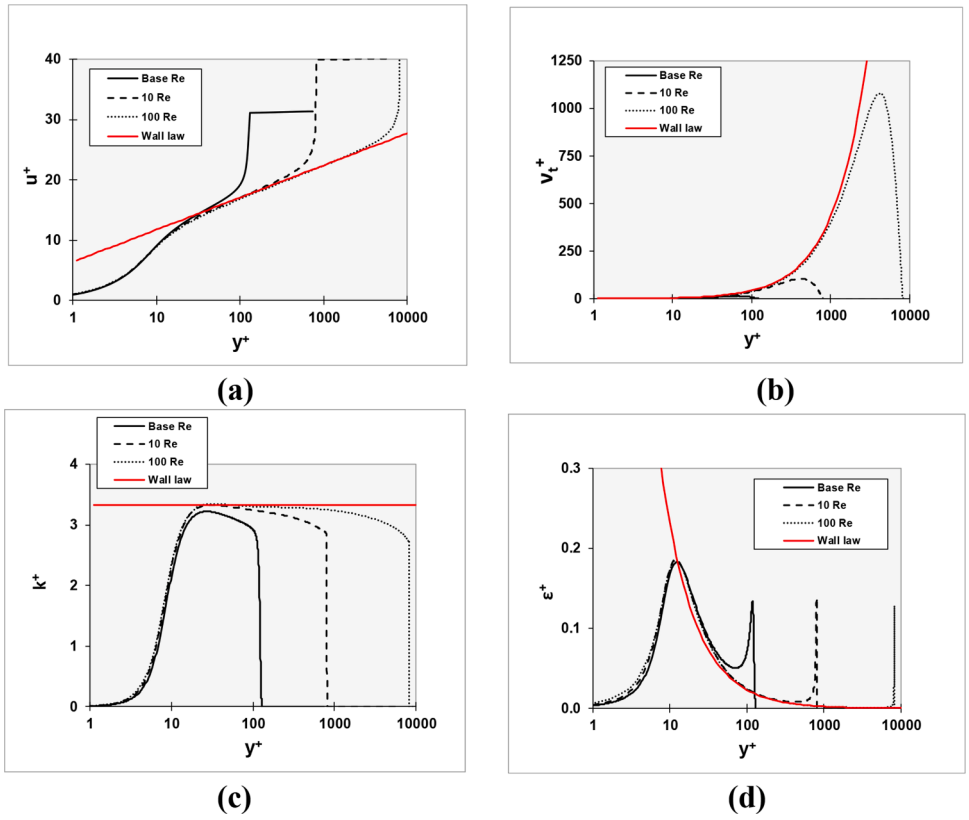

Fig. 5. Turbulent scaling in the inertial sublayer of the water annulus (applying the 1D model); (a) streamwise velocity, $u^+ = u/u_\tau$, (b) turbulent viscosity, $\nu_t^+ = \nu_t / \nu_w$, (c) turbulent kinetic energy, $k^+ = k/u_\tau^2$, (d) turbulent dissipation rate, $\epsilon^+ = \tilde{\epsilon}\nu_w/u_\tau^4$.

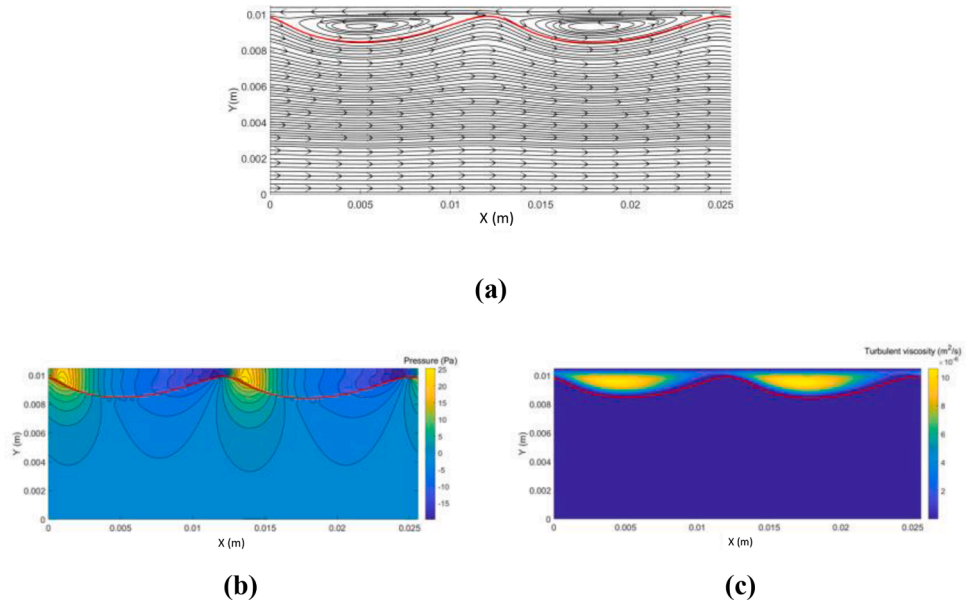

Fig. 6. 2D results with respect to observer that travels with the wave velocity of 1.24 m/s; (a) streamlines, (b) isobars, (c) turbulent viscosity.

with respect to the oil core, the wave crest is at the location where the water annulus is thinnest and the wave trough is at the location where the water annulus is thickest. With respect to the travelling wave, there is a recirculation zone of water in between the wave trough and crest locations. Turbulence is highest at the wave trough location (thickest water annulus, giving highest local shear-based Reynolds number) and lowest at the wave crest location (thinnest water annulus, giving lowest local shear-based Reynolds number). At a certain streamwise location, the pressure is almost constant across the thickness of the water annulus.

Fig. 7 shows the pressure at the pipe wall and at the oil-water interface, along with the thickness of the water annulus. This is done both at a certain time in spatial direction (left graph) and at a certain streamwise location over time (right graph). The two graphs can be converted into one another by using the 1.24 m/s wave velocity. The figure confirms that the wall pressure and interface pressure are very close. The pressure is largest at the location where the dividing

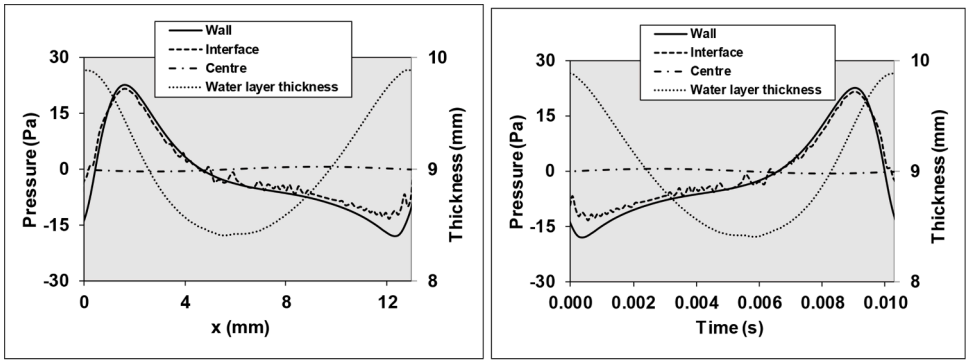

Fig. 7. 2D simulation results for the pressure distribution; (a) spatial (flow is from left to right), (b) temporal.

streamline of the recirculation zone reattaches at the interface (which can be seen as the windward side of the interface) and pressure is lowest at the location where the dividing streamline of the recirculation zone leaves the interface (which can be seen as the leeward side of the interface). Through integrating the pressure along the interface in x-direction the form drag working on the wave interface can be determined. The shear-stress force on the interface in x-direction can be determined from a force balance (using the wall shear stress force, the driving pressure force, and the form drag). It turns out that 68% of the interface force is due to pressure (form drag) and 32% due to shear stress. Fig. 7 also shows that the pressure at the oil core centre is almost constant. As the pressure jump across the interface due to the interface tension is 4 Pa at most (at locations with the highest interface curvature), the fluctuations in the interface pressure (of about 20 Pa) are also felt in the oil core. This will lead to (small) secondary flow in the oil core.

As shown in Fig. 8, there is a very good agreement for the frequency and amplitude of the interfacial waves as obtained in the 2D simulations and in the lab experiments. This will be discussed further in the next sections, which will also include the 3D simulation results.

5. 3D results

5.1. Simulation set-up

3D simulations were carried out for cases without and with gravity. Without gravity, the oil core remains concentric in the pipe, but a symmetry breaking of the interface has appeared, as compared to the results obtained with the 2D axi-symmetric model (but the flow characteristics remain fairly close to the 2D results). When the gravity is added, the oil core becomes eccentric, with a water annulus that is thinner at the top than at the bottom. Some dispersion of oil droplets in the bottom water layer occurs; these oil droplets make up about 0.3% of the oil volume in the oil core.

In the 3D simulations with gravity a pressure drop of 725 Pa/m was prescribed, along with a water holdup fraction of 0.257, which gave a total volumetric flow rate of 0.00047 m^3/s and a watercut of 20% (which are close to the value set in the experiments, being 0.00043 m^3/s total flow rate and 20% watercut). The pressure drop and water holdup fraction were used as boundary conditions in the 3D simulations, as this is computationally much more convenient than prescribing the total flow rate and the watercut. Note that the 3D simulations (on a rather fine mesh) require a large computational time. It would have been better to iterate the conditions for the pressure drop to obtain a flow rate precisely equal to the experimental value (while maintaining the 20% watercut), but this was not done because of the available computer resource capacity.

Although the flow rate in the 3D simulation (with gravity) is slightly higher than in the experiments (by 9%), the pressure drop is still 34% lower (725 Pa/m instead of 1100 Pa/m). Thus, switching from 2D to 3D does not imply a pressure drop value closer to the experimental value.

5.2. Turbulence characteristics

The (spatially and temporally averaged) values of the turbulent viscosity (scaled with the water viscosity) over the cross section of the pipe are shown in Fig. 9. Shown are the values obtained by averaging both in time and in streamwise spatial direction. Both the results with gravity and without gravity are depicted. Without gravity, the (time and space averaged) oil core is concentric and circular (i.e. axi-symmetric). The water annulus is turbulent (as $\nu_t/\nu_w > 1$) and the oil core is laminar

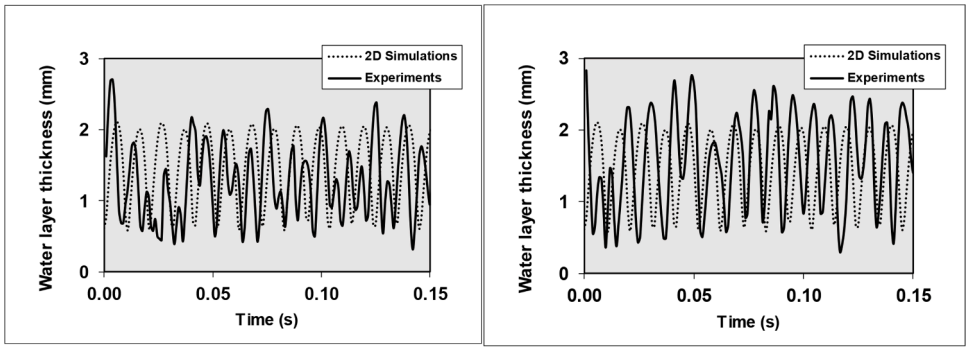

Fig. 8. Comparison of 2D results with experiments for the thickness of the water annulus; (a) top layer, (b) bottom layer.

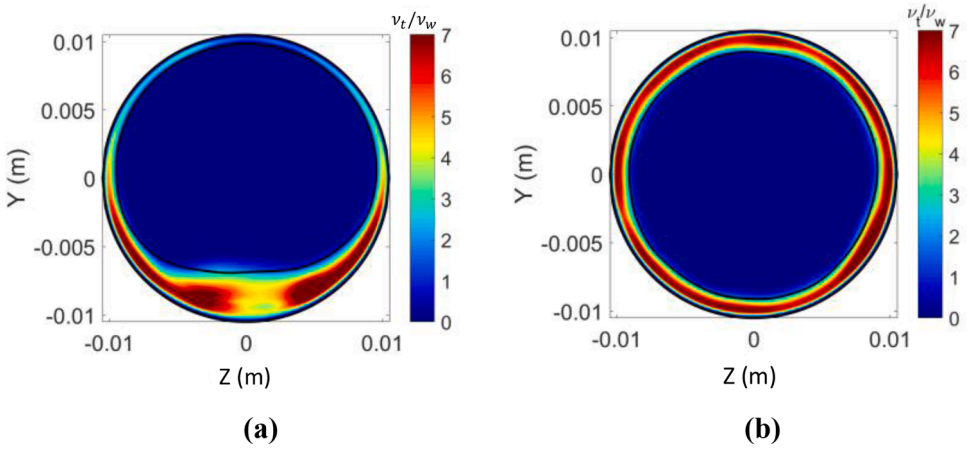

Fig. 9. Comparison of the turbulent viscosity (scaled with the water viscosity) for the 3D simulation; (a) with gravity, (b) without gravity. Values are averaged over time and along the main flow direction. The oil-water interface is indicated with a solid black line.

(almost zero turbulent viscosity). When gravity is added, the oil core rises giving a thinner water annulus at the top and a thicker water annulus at the bottom. As a consequence (compared to the concentric core without gravity), the turbulent viscosity decreases in the top layer and increases in the bottom layer.

What follows here is for the case with gravity. The relation between the turbulence and the water annulus thickness is also clear from the temporal fluctuations at a fixed streamwise location, as is shown in Fig. 10. The frequency of the oscillation in the top layer is about double that of the bottom layer. The turbulence in the top layer is very low, whereas the bottom layer shows an oscillation between full turbulence at the wave trough and a tendency to relaminarization at the wave crest.

A snapshot of the turbulence profiles in the bottom layer at the location where the water annulus is thickest (wave trough) is shown in Fig. 11. For comparison, also the 1D and 2D simulation results are included. All quantities are non-dimensionalized with the wall shear velocity u_τ and the kinematic water viscosity ν_w. Also the asymptotic wall layer layers (see Section 3) are included. There is a close agreement between the scaled velocity profile as found in the 1D, 2D, and 3D simulations. Note the maximum value of u^+ (which denotes the bulk oil core velocity) is different for the 1D, 2D, and 3D results; this is because of the difference in wall shear stress near the pipe wall. Very close to the wall, which is in the viscous sublayer, we have $u^+ = y^+$. In the inertial sublayer, i.e. between about 10 and 100 in these simulations, the turbulence profiles are fairly close to the law-of-wall curves, which demonstrates that full turbulence (i.e. vanishing effect of the low-Reynolds number terms in the $k-\epsilon$ model) has been reached.

5.3. Levitation mechanism

The density difference between the water and oil, in the presence of gravity in horizontal CAF flow, will cause the oil core to move upward, giving an eccentricity. To study this levitation mechanism due to the presence of gravity, the forces acting on the oil core will be analysed. See the sketch with definitions in Fig. 12. The index 2 denotes the wall location and S_2 is the pipe wall. Furthermore, w represents water and o represents oil, $\vec{n}$ is the surface normal vector, ρ is the density, g is the gravitational acceleration, V is the volume, p is pressure and τ is shear stress.

The total force on the oil core in our simulation can also be calculated as:

$$F_y^{core} = \frac{d}{dt}\int_{V_o} \rho_o v \, dV \tag{26}$$

This total force acting on the oil core, as derived from the 3D simulation results, is shown in Fig. 13. In the first part of the transient simulation ($t < 0.25$ s), which starts with a concentric oil core, the total force is positive, due to the upward buoyancy, and the oil core moves upward. Then, in the time interval 0.13 s $< t <$ 0.25 s (as indicated in the figure), the total force on the core is negative, acting downward. This is the stage during which the eccentric core is decelerated and its upward velocity is reduced. The downward force is related to waves which are created at the oil-water interface. After 1 s, when the levitation of the core has become stable, the total force acting on the oil core shows a small oscillation around zero.

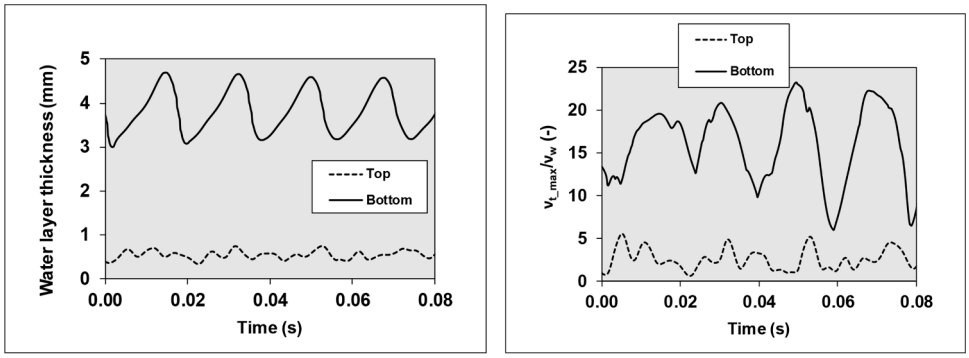

Fig. 10. Temporal fluctuation at fixed streamwise location in 3D simulation; (a) water layer thickness, (b) maximum in the turbulent viscosity.

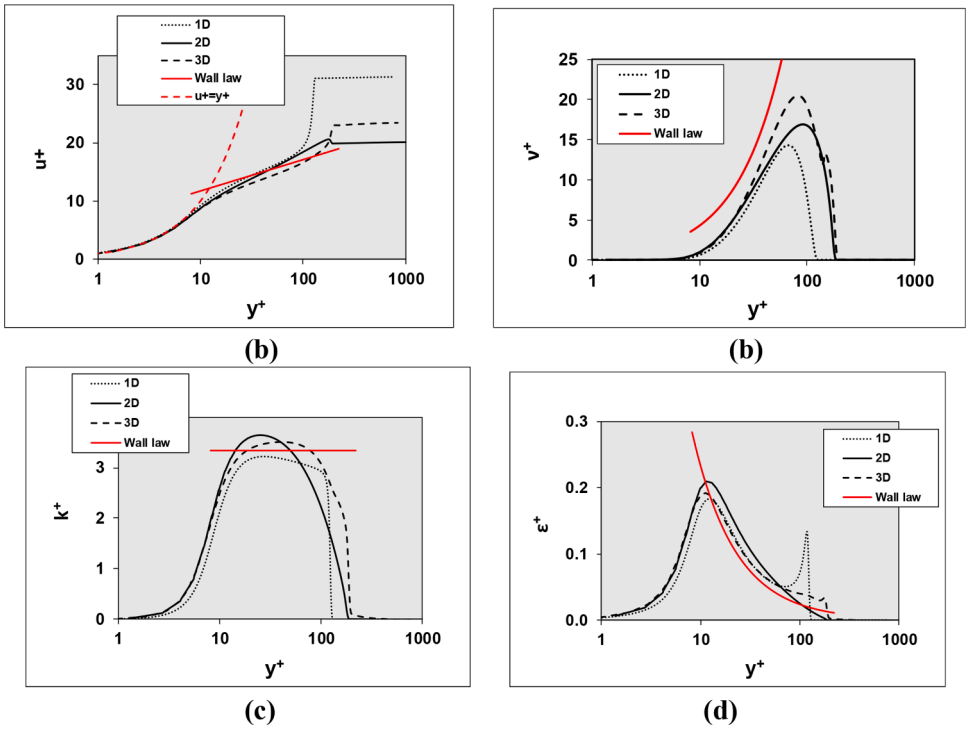

Fig. 11. Instantaneous quantities as function of the scaled distance to the wall at the location of the thickest water annulus along the bottom (wave trough); (a) streamwise velocity, $u^+ = u/u_\tau$, (b) turbulent viscosity, $\nu_t^+ = \nu_t/\nu_w$, (c) turbulent kinetic energy, $k^+ = k/u_\tau^2$, (d) turbulent dissipation rate, $\epsilon^+ = \tilde{\epsilon}\nu_w/u_\tau^4$.

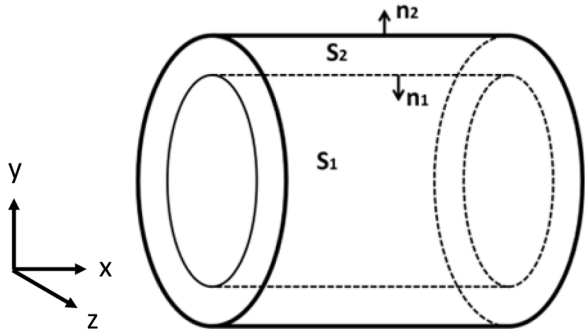

Fig. 12. Definition of the surfaces and the normal vectors.

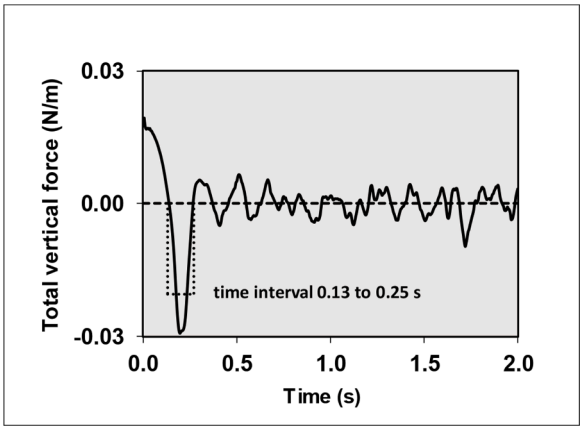

Fig. 13. Total upward force (per meter pipe length) acting on the oil core as a function of time.

The levitation mechanism of CAF has been studied by several researchers (albeit in the presence of a laminar water annulus). By neglecting inertia, Ooms et al. (1984) developed the lubricated-film model, in which the viscous force acting on the core surface balances the buoyancy force. This model is applied with a saw tooth shaped interface. Bai et al. (1992) claimed that the lubrication force and the inertia force might coexist in core-annular flow. Under the effect of the inertia force, the wave shape will become more rounded. Clearly under the present conditions with a Reynolds number that gives turbulent flow in the water annulus, the inertia terms are important (as they lead to the Reynolds stresses in the RANS equations, as modelled by the $k-\epsilon$ model). To study the wave forces, the reduced pressure is used in this study: ϕ_2 is defined as the hydrodynamic pressure without the hydrostatic contribution due to water:

$$\phi_2 = p_2 + \rho_w g y \tag{27}$$

Then the total resulting force (which gives the acceleration) acting on the oil core can be split as:

$$F_y^{core} = \underbrace{\int_{S_1} (\phi_2)_{S_1} n_{1,y} dS_1}_{\Phi_y^{core}} + \underbrace{\int_{S_1} \left(-\tau_{2,yk}^{(v)} \right) n_{1,y} dS_1}_{T_y^{core}} + \underbrace{\left(\int_{S_1} (-\rho_w g y)_{S_1} n_{1,y} dS_1 - \rho_o g V_o \right)}_{B_y^{core}} \tag{28}$$

S_1 is the oil-water interface (which has $\alpha = 0.5$), n_1 is the normal vector at the oil-water interface, calculated from the volume fraction α:

$$n_1 = \frac{\nabla \alpha_1}{|\nabla \alpha_1|} \tag{29}$$

The first and second terms on the right hand side of Eq. (28) are the reduced pressure force Φ_y^{core} and the viscous stress T_y^{core} acting on the core, respectively, and the third term is the buoyancy force for the core B_y^{core}.

The reduced pressure force, the viscous force, and the buoyancy

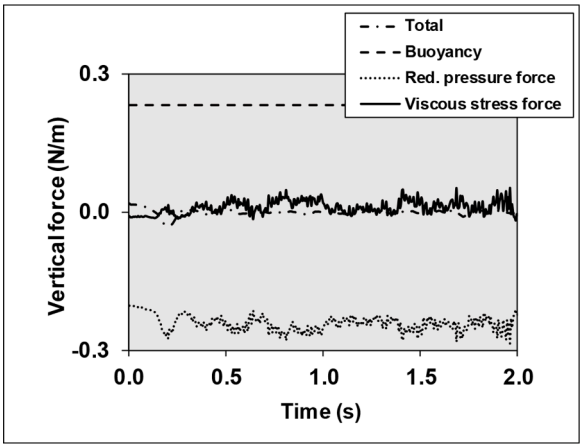

Fig. 14. Reduced pressure force, shear stress force, buoyancy force, and resulting force for the oil core as a function of time; note that the vertical axis shows the force per meter pipe length.

force, all working on the oil core, are shown in Fig. 14. Here the minus sign denotes that the force is acting downwards.

Under the influence of gravity, a secondary flow will be induced by the flow dynamics. To obtain the main characteristics of the secondary flow, the velocity is averaged both in time and in streamwise spatial direction. In this way a 2D velocity field is obtained. When the oil core is moving upward in the time-dependent flow with traveling waves at the oil-water interface, a downflow of water will be induced in the water annulus at the left and right sides. Due to the wave motion the oil core will locally move continuously up and down over time. After averaging, non-zero values of the velocity in the 2D velocity field are found.

The resulting averaged streamlines are shown in Fig. 15a, where the colour represents the velocity magnitude. Due to the averaging, a (nearly) symmetric flow pattern is obtained. The maximum in the (averaged) secondary flow velocity is 0.014 m/s, which is around 1% of the oil core velocity. The maximum is found in the water annuli at the left and right sides. The velocity magnitude in the top and bottom layer is small. Fig. 15b shows the azimuthal velocity at various angles. As can be seen, a shear flow exists at the left and right hand side of the pipe. The water close to the pipe wall is flowing downward and the water close to the interface with the oil core flowing upward. In the bottom layer, two symmetric vortices, with opposite rotation direction, exist. The secondary flow velocity is also large near to these vortices. A higher turbulent viscosity exists in these recirculation zones. At the very bottom part, the streamlines show more recirculation zones but the velocity magnitude is small. This is where some dispersed oil droplets float in the water layer. Fig. 15c shows the isobars for the reduced pressure. The reduced pressure is higher in the top water layer than in the bottom water layer. The pressure difference between the top and bottom compensates the buoyancy force on the oil core. This will be discussed in more detail in the next subsection.

5.4. *Interfacial waves*

As discussed in the previous subsection, the (reduced) pressure plays a major role in the levitation of the oil core. The build-up of the pressure is closely related to the waves at the oil-water interface. To determine the wave velocity from the 3D results, the time dependent oscillation of the thickness of the water annulus was monitored at two very close streamwise locations and the time shift was determined. The ratio of distance between the locations and the time shift gives the wave

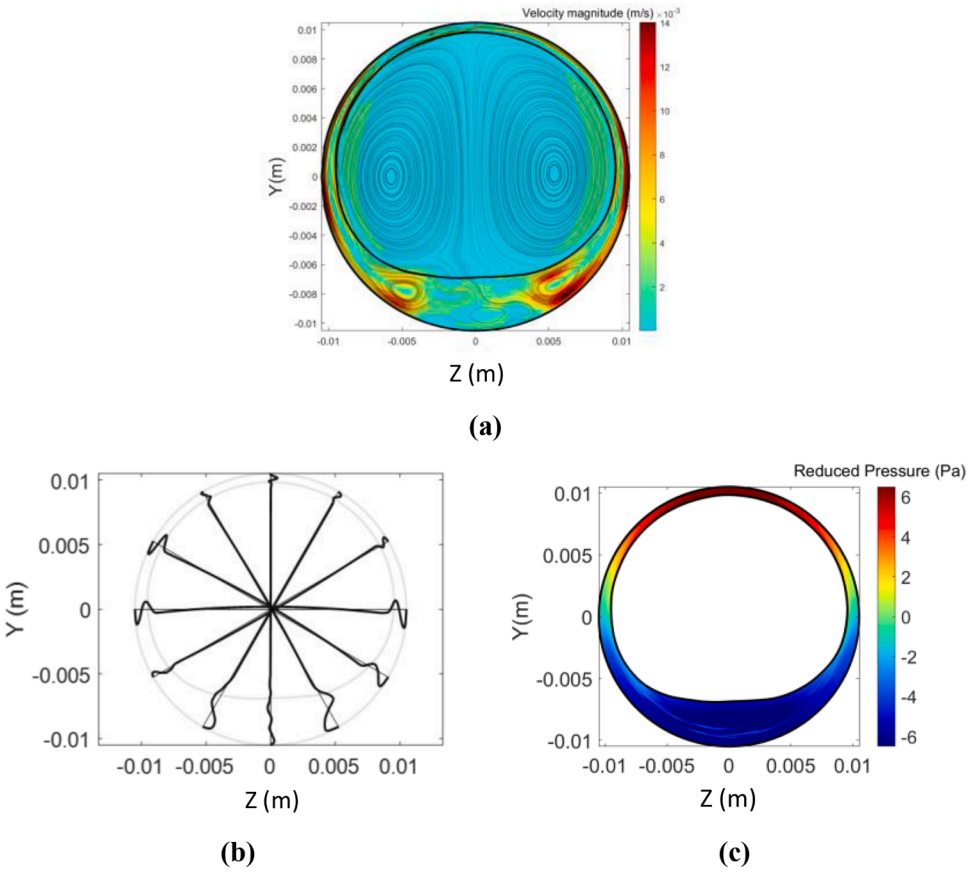

Fig. 15. Flow in 2D plane obtained after averaging; (a) streamlines, (b) azimuthal velocity distribution at different angle locations, (c) contours of the reduced pressure.

velocity. This wave velocity is determined at the 3, 6, 9, and 12 o'clock locations around the perimeter. At a certain location along the perimeter, the wave velocity is almost constant (i.e. independent of the local water layer thickness), which means that the spatial wave movement and the temporal wave oscillations can be converted into each other by this fixed wave velocity. This wave velocity is about 1.2 m/s for the top wave and about 1.43 m/s for the bottom wave; this is comparable to the average velocity of 1.33 m/s in the oil core.

Fig. 16 shows the instantaneous fluctuation in the pressure along the interfacial wave in the mid plane. The fluctuation is obtained by subtracting the time averaged pressure from the instantaneous value. The secondary flow velocity (which is the velocity after subtraction of the mean oil core velocity) is shown as streaklines in the same figure. The figure shows that the pressure fluctuates most at the top interface. At the bottom interface, there is less fluctuation. The streaklines show that there is flow recirculation in the wave trough in the bottom layer.

Fig. 17 shows the reduced pressure distribution along the top and bottom water annuli. Both the temporal and spatial dependence are shown. In fact the temporal result was mapped to the spatial distribution by using the fixed wave velocity; therefore, the spatial length in the figure is longer than the 25.6 mm used in the simulation.

As was already shown in Fig. 10a for the 3D simulation results, the interfacial waves at the top have a wave length of about one-third (8.5 mm) of the waves at the bottom (25.6 mm). Due to the eccentricity, the average thickness of the water annulus at the top (0.6 mm) is much thinner than at the bottom (3.6 mm). As the water annulus is much thinner at the at the top, here the pressure reacts stronger on passing waves than at the bottom. This explains the difference in fluctuations in the reduced pressure, as shown in Fig. 17. When comparing the pressure distribution with the location of the wave crests and troughs, it is seen again (similar to the 2D results) that the pressure is highest on the windward side of the interface and lowest at the leeward side of the interface. Through integrating the pressure along the interface in x-direction the form drag working on the wave interface can be determined. It turns out that 48% of the interface force is due to pressure (form drag) and 52% due to shear stress. This is the average for the total interface (i.e. all around the perimeter and along the length of the pipe section). The form drag strongly depends on the location at the interface: it is much smaller along the bottom interface (where the reduced pressure is fairly flat) compared to the top layer (where the reduced pressure shows a strong fluctuation).

From Fig. 17 it is clear that the value of the reduced pressure in the top layer is almost always and everywhere higher than at the bottom layer. This gives a net downward force on the oil core, which counter balances the upward buoyancy force and prevents the oil from fouling the top wall. The figure also shows that the reduced pressure is fairly flat along the interface at the bottom layer, whereas it shows strong fluctuations along the top layer. This can be related to the amplitude of the waves along the bottom interface and along the top interface (see Fig. 10): a thick water annulus with relatively large amplitude waves at the bottom and a thin water layer with small amplitude waves along the bottom. The amplitude of the waves at the bottom is so large that the water flow easily separates at almost the location of the wave crest, which gives almost parallel flow and thus almost no pressure change. This is in contrast to the top layer where the water flow follows the interface over a longer distance before it separates and reattaches, leading to the significant pressure fluctuations. The net effect is a "flying core flow" (as described by Joseph et al, 1997) with downward lift that counterbalances the upward buoyancy.

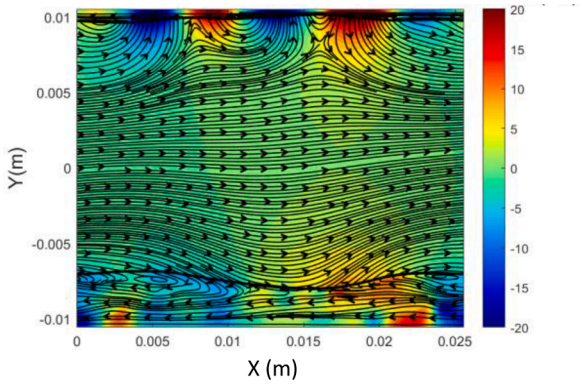

Fig. 16. Snap shot of the pressure fluctuation in the mid plane, as well as streak lines of the secondary flow. The oil-water interface is represented by a thick black line.

6. Comparison of simulations with experiments

Table 2 compares the results from the CFD simulations with the experiments obtained in our lab. For the simulations, both the 2D and 3D results are considered. In the experiments the total flow rate and watercut were prescribed, and the output parameters pressure drop and water holdup fraction were obtained. In the 2D simulations (i.e. axisymmetric, no gravity), the total flow rate and the water holdup fraction were prescribed, and the pressure drop and watercut followed as output. In the 3D simulations (with gravity) the pressure drop and water holdup fraction were prescribed, and the total flow rate and watercut followed as output. To make a most meaningful comparison, it is best to use scaled quantities to represent the flow rate and pressure drop on one hand, and the watercut and water holdup fraction on the other hand; chosen are the pressure drop reduction ratio (R_p) and the holdup ratio (h). The pressure reduction ratio is defined as the ratio between the pressure drop for single phase flow at the given oil flow rate and the water/oil pressure drop. The single phase oil flow will be laminar and has the well know pressure drop for Poiseuille flow:

$$-\frac{dP_{oil}}{dx} = \frac{128}{\pi}\frac{\nu_{oil}\rho_{oil}Q_o}{D^4} \tag{30}$$

The holdup ratio was already defined by Eq. (21).

The table shows that the pressure drop reduction factor for the 2D and 3D results is about the same, but its value is about 35% higher than in the experiment (or, at the same oil flow rate, the predicted pressure drop is about 35% lower than in the experiment).

A hold-up ratio larger than 1 corresponds to the relative accumulation of water (giving a lower bulk water velocity than the bulk oil velocity), which can be explained by the encapsulation of water in the troughs of the interfacial waves. Bai et al. (1992) performed an experimental study of vertical core-annular flow; it was found that in cases with high flow, for both upward and downward CAF, the hold-up ratio is always equal to 1.39, independent of the oil and water flow rates. In the present study for horizontal CAF, the hold-up ratio in the 3D model (h=1.38) is close to the experimental value (h=1.41), but the 2D prediction is slightly lower (h=1.23). Therefore, the apparent slip between the oil and water (due to the interfacial stress) in the 3D simulation agrees with the experiment, but the 2D simulation gives a too low slip (or too much interfacial stress).

It is also meaningful to compare the location of the oil core and the structure of the interfacial waves (wave amplitude, wave length, wave velocity). Fig. 18 shows the average location of the water-oil interface, which also reveals the eccentricity of the oil core. The eccentricity factor is defined as the half the difference between thickness of the water annulus at the bottom and the top, scaled with the pipe radius. As shown in the figure (and in Table 2), there is only very little eccentricity in the experiment, whereas the 3D simulation gives much eccentricity (bottom water layer is much thicker than the top water layer). Comparison of the water layer thickness and the wave amplitude in Table 2 reveals a good agreement between the 2D predictions and the experiments, but larger deviations between the 3D predictions and the experiments. The 2D and 3D results for the wave velocity and wave length (and for the wave

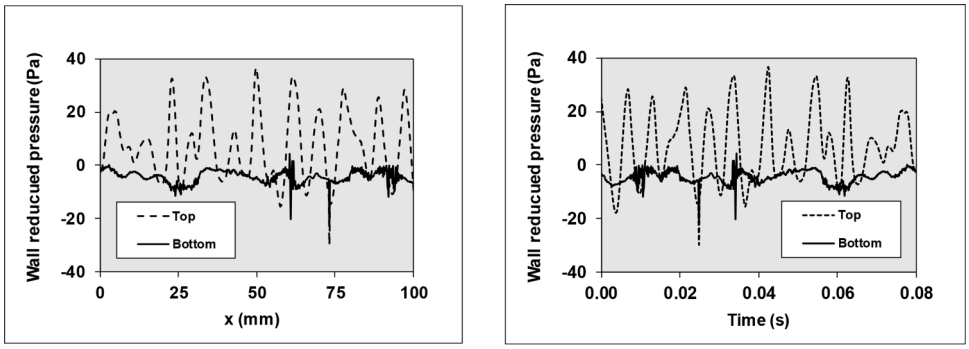

(a) (b)

Fig. 17. 3D simulation results for the reduced pressure distribution for the bottom and top layers; (a) spatial (flow is from left to right), (b) temporal.

Table 2
Comparison of the results.

		Experiment	2D simulation	3D simulation
Total flow rate	m^3/s	0.00043	0.00043	0.00047
Water hold up fraction		0.26	0.257	0.257
Water cut	%	20	22	20
Pressure drop	Pa/m	1120	748	725
Hold up ratio (h)		1.41	1.23	1.38
Press. Drop red. factor (R_p)		45	65	76
Eccentricity Factor		0.014	0.000	0.145
Water layer thickness:				
Left	mm	1.48	1.49	1.22
Right	mm	0.96	1.49	1.04
Top	mm	1.24	1.49	0.57
Bottom	mm	1.53	1.49	3.62
Wave amplitude:				
Left	mm	0.83	0.73	0.48
Right	mm	1.09	0.73	0.46
Top	mm	0.78	0.73	0.19
Bottom	mm	1.13	0.73	0.65
Wave length:				
Left	mm	11.4	12.8	12.8
Right	mm	10.7	12.8	12.8
Top	mm	10.8	12.8	8.5
Bottom	mm	11.8	12.8	25.6
Wave Velocity:				
Left	m/s	1.3	1.24	1.33
Right	m/s	1.37	1.24	1.33
Top	m/s	1.37	1.24	1.2
Bottom	m/s	1.21	1.24	1.43

frequency) are in good agreement with the experiments. An exception is the wave length in the bottom layer of the 3D results: this wave length is double the measured value.

The comparison shows that there are remarkable differences between the simulations and the lab experiments: the predicted pressure drop reduction factor is significantly higher in the simulation than in the experiments and the eccentricity predicted by the 3D simulations is much higher than in the experiment. Due to the low eccentricity in the experiment, the 2D axi-symmetric simulation results (i.e. zero eccentricity) for the interfacial waves are in better agreement with the flow visualization in the experiments than the 3D results.

The observed differences can be due to limitations of using a low-Reynolds number $k-\epsilon$ model. Such a model is expected to work well for attached wall-bounded flow, as the model parameters in the original model formulation have been tuned to properly describe the viscous sublayer and the intertial sublayer of such flows. The model will be less good in describing flow separation and the extent of recirculation zones, where using a differential stress model (within the RANS approach)

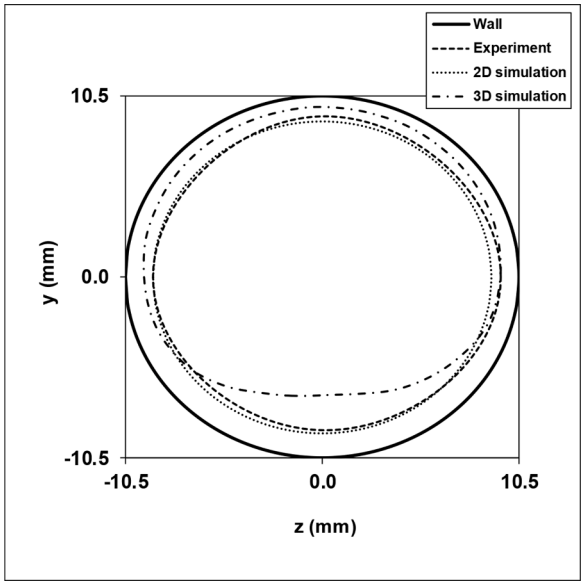

Fig. 18. Average location of the water-oil interface.

instead of a two-parameter model like $k-\epsilon$ should be used. A low-Reynolds number $k-\epsilon$ model will also be less good in describing laminar-turbulent transition, such as in flows with relaminarization periods or zones. The considered water annulus in the present study has all three flow features: wall bounded flow along the pipe wall, flow separation with recirculation along the wave water-oil interface, relaminarization tendency if the water layer becomes too thin.

Using DNS for single phase channel flow, Jiménez and Moin (1991) (see also Rocco et al., 2019, 2021) have shown that a minimum value of about 90 is needed for $Re_\tau = d^+ = u_\tau d/\nu_w$ to have sustained turbulent flow. Fig. 19 shows Re_τ and $\nu_{t,max}/\nu_w$ for the current 1D, 2D, and 3D simulations. It shows that full turbulence has been reached in the 1D and 2D simulations, and in the bottom layer of the 3D simulation, but not in the top layer where a tendency to relaminarization is found. It is very well possible that the relaminarization in the top layer with sustained turbulent flow in the bottom layer is responsible for the relatively large eccentricity in the 3D simulation. Sustained turbulent flow in the top layer may lead to a reduced eccentricity, as found in the experiments.

7. Conclusions

1D, 2D, and 3D numerical simulations were performed for horizontal core-annular flow (CAF) with a turbulent water annulus. Thereto, the Reynolds-Averaged Navier-Stokes (RANS) equations were solved with

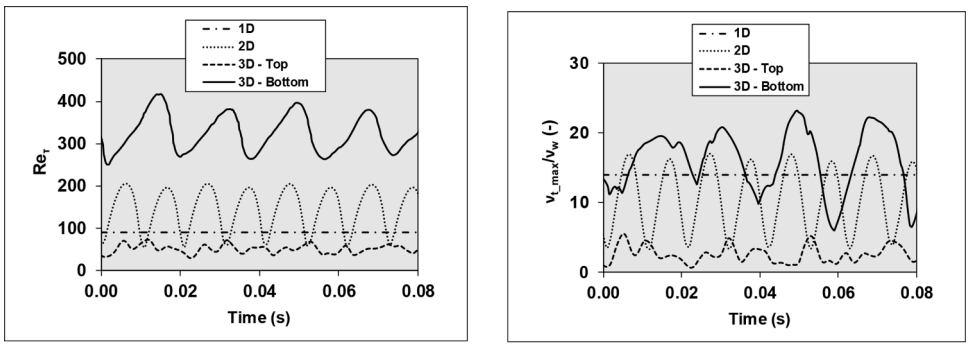

Fig. 19. Comparison of simulation results; (a) shear-based Reynolds number (Re_τ), (b) scaled maximum turbulent viscosity ($\nu^+_{t,max} = \nu_{t,max}/\nu_w$).

the low-Reynolds number Launder & Sharma $k-\varepsilon$ model for the turbulence. The base case is the flow in a 21 mm diameter pipe with oil and water that have a viscosity ratio of 1150 and a density ratio of 0.91. The flow is characterized by travelling waves at the oil-water interface. The oil core is laminar, and the water annulus is turbulent. The simulation results were compared with experiments (pressure drop measurements, flow visualization) obtained in our lab. To verify the good numerical accuracy of the simulation results, the simulations were repeated on successively refined meshes. Obviously, it is important to have a sufficient number of numerical grid points close to the wall in the viscous sublayer, as well as in the wavy interfacial zone.

The 1D results represent perfect turbulent CAF (i.e. no gravity, no interfacial waves), the 2D results represent axi-symmetric CAF (i.e. no gravity, with interfacial waves). And the 3D results represent eccentric CAF (i.e. with gravity, with interfacial waves). The simulation results typically show a turbulent water annulus in which the structure of the (high-Reynolds number) inertial sublayer can be recognized. The inertial sublayer scaling (using wall units) was demonstrated to be present for the streamwise velocity, for the turbulent viscosity, for the turbulent kinetic energy, and for the turbulent energy dissipation. However, as the shear-based Reynolds number is limited, also the extent of the inertial sublayer is limited.

The 2D and 3D results for the interfacial waves show that the waves are travelling with a practically constant wave velocity. This means that the temporal and spatial results can be converted into one another using this convective velocity. It also means that an observer traveling with the waves will see an almost steady flow. The turbulence is highest at the streamwise location where the water annulus is thickest (i.e. at the trough location of the wave) and lowest at the location where the water annulus is thinnest (i.e. at the crest location of the waves). With respect to the travelling waves, a water recirculation zone is found in between the successive crest locations. Monitoring the pressure along the interface, the pressure is largest at the location where the dividing streamline of the recirculation zone reattaches at the interface (which can be seen as the windward side of the interface) and pressure is lowest at the location where the dividing streamline of the recirculation zone leaves the interface (which can be seen as the leeward side of the interface). Through integrating the pressure along the interface in streamwise direction the form drag working on the wave interface can be determined. For the 2D results, 68% of the interface force is due to pressure (form drag) and 32% due to shear stress. For the 3D results we find 48% form drag and 52% shear stress force.

A force balance on the oil core was performed for the 3D results to determine the levitation in vertical direction. Thereto, the total force is split into a reduced pressure force, viscous force and buoyancy force. It is found that during the initial stage of the transient simulation (which starts with a concentric oil core), the reduced pressure force and the viscous force at the oil-water interface are both acting in opposite direction to the buoyancy force; these two forces together grow larger than the buoyancy force, creating a downward resulting force on the oil core. The levitation mechanism is closely related to the shape of the interfacial waves. The amplitude of the waves at the bottom is such large that the water flow easily separates at almost the location of the wave crest, which gives almost parallel flow and thus almost no pressure change in streamwise direction. This is in contrast to the top layer where the water flow longer follows the interface before it separates and reattaches, leading to the significant pressure fluctuations. Almost everywhere the reduced pressure along the top interface is higher than at the bottom interface, which provides the downward force in line with the flying-core concept (downward lift) described by Joseph et al. (1997).

There are significant differences between the simulation results and the lab experiments. The pressure drop reduction factor (which is the ratio between the pressure drop for CAF and the pressure drop for single phase viscous oil flow) for the 2D and 3D results is about the same, but its value is about 35% higher than in the experiment (or, at the same oil flow rate, the predicted pressure drop is about 35% lower than in the experiment). The hold-up ratio in the 3D model (h=1.38) is close to the experimental value (h=1.41), but the 2D prediction is slightly lower (h=1.23). Therefore, the apparent slip between the oil and water (due to the interfacial stress) in the 3D simulation agrees with the experiment, but the 2D simulation gives a too low slip (or too much interfacial stress). The 2D and 3D results for the wave velocity and wave length (and for the wave frequency) are in good agreement with the experiments. An exception is the wave length in the bottom layer of the 3D results: this wave length is double the measured value. The eccentricity predicted by the 3D simulations is much higher than in the experiment. Due to the low eccentricity in the experiment, the 2D axi-symmetric simulation results (i.e. zero eccentricity) for the interfacial waves are in better agreement with the flow visualization in the experiments than the 3D results.

Most likely, the observed differences between the simulations and the experiments are due to limitations of using a low-Reynolds number $k-\epsilon$ model. Such a model is suited for attached wall-bounded flow, but less good for flow separation with recirculation and for relaminarization. For fully turbulent flow a shear-based Reynolds number Re_τ of at least about 90 is needed. Full turbulence has been reached in the 1D and 2D simulations, and in the bottom layer of the 3D simulation, but not in the top layer where a tendency to relaminarization is found. It might be that the relaminarization in the top layer with sustained turbulent flow in the bottom layer is responsible for the relatively large eccentricity in the 3D simulation. Additional experiments and simulations are needed to further verify this. With respect to the experiments one can think of more detailed measurements of the flow in the water annulus (e.g. using Particle-Image Velocimetry). Also using a larger pipe diameter (which gives a thicker, more turbulent water annulus) would be helpful. This

increases the Re_τ value in the experiments, which would probably make the conditions easier for simulation with a low-Reynolds number $k-\epsilon$ model. Additional 3D simulations with a higher Re_τ could be carried out to verify its effect on the eccentricity. Repeating the simulations for the current conditions with a LES approach, or even with a DNS approach, is also recommended.

CRediT authorship contribution statement

Haoyu Li: Investigation, Writing – original draft. **M.J.B.M. Pourquie:** Supervision, Writing – review & editing. **G. Ooms:** Supervision, Writing – review & editing. **R.A.W.M. Henkes:** Supervision, Writing – review & editing.

Declaration of Competing Interest

The authors declare that they have no known competing financial interests or personal relationships that could have appeared to influence the work reported in this paper.

Acknowledgement

The first author has received a grant from the China Scholarship Council(CSC). Thanks are also due the Netherlands Foundation of Scientific Research (NWO) for supplying the computer time.

References

Archibong-Eso, A., Shi, J., Baba, Y.D., Aliyu, A.M., Raji, Y.O., Heung, H., 2017. High viscous oil–water two–phase flow: experiments & numerical simulations. Heat Mass Transf. 55, 755–767.
Arney, M.S., Bai, R., Guevara, E., Joseph, D.D, Liu, K., 1993. Friction factor and holdup studies for lubricated pipelining-I. Experiments and correlations. Int. J. Multiphase Flow 19, 1061–1076.
Bai, R., Chen, K., Joseph, D.D., 1992. Lubricated pipelining: stability of core-annular flow. part 5. Experiments and comparison with theory. J. Fluid Mech. 240, 97–132.
Bannwart, A.A., 2001. Modeling aspects of oil-water core-annular flows. J. Petrol. Sci. Eng. 32, 127–143.
Beerens, J.C., Ooms, G., Pourquié, M.J.B.M., Westerweel, J., 2014. A comparison between numerical predictions and theoretical and experimental results for laminar core-annular flow. AIChE J. 60, 3046–3056, 8.
Chen, K., Bai, R., Joseph, D.D., 1990. Lubricated pipelining. Part 3 Stability of core-annular flow in vertical pipes. J. Fluid Mech. 214, 251–286.
Ghosh, S., Mandal, T.K., Das, P.K., 2009. Review of oil water core annular flow. Renewable Sustainable Energy Rev. 13, 1957–1965.
Hasson, D., Mann, V., Nir, A., 1970. Annular flow of two immiscible liquids I. Mechanisms. Can. J. Chem. Eng. 48, 514–520.
Henkes, R.A.W.M., 1998. Scaling of the turbulent boundary layer along a flat plate according to different turbulence models. Int. J. Heat Fluid Flow 19, 338–347.
Huang, A., Christodoulou, C., Joseph, D.D., 1994. Friction factor and holdup studies for lubricated pipelining - II; laminar and k-ϵ models of eccentric core flows. Int. J. Multiphase Flow 20, 481–491.
Huang, A., Joseph, D.D., 1995. Stability of eccentric core–annular flow. J. Fluid Mech. 282, 233–245.
Jiménez, J., Moin, P., 1991. The minimal flow unit in near-wall turbulence. J. Fluid Mech. 225, 213–240.
Joseph, D.D., Bai, R., Chen, K.P., Renardy, Y.Y., 1997. Core-annular flows. Ann. Rev. Fluid Mech. 29, 65–90.
Kim, K., Choi, H., 2018. Direct numerical simulation of a turbulent core-annular flow with water-lubricated high viscosity oil in a vertical pipe. J. Fluid Mech. 849, 419–447.
Ko, T., Choi, H.G., Bai, R., Joseph, D.D., 2002. Finite element method simulation of turbulent wavy core-annular flows using a k-ω turbulence model method. Int. J. Multiphase Flow 29, 1205–1222.
Launder., B.E., Sharma, B.T., 1974. Application of the energy dissipation model of turbulence to the calculation of flow near a spinning disc. Lett. Heat Mass Transf. 1, 131–138.
Li, J., Renardy, Y., 1999. Direct simulation of unsteady axisymmetric core–annular flow with high viscosity ratio. J. Fluid Mech. 391, 123–149.
Preziosi, L., Chen, K., Joseph, D.D., 1989. Lubricated pipelining: stability of core-annular flow. J. Fluid Mech. 201, 323–356.
Ooms, G., Segal, A., Van der Wees, A.J., Meerhoff, R., Oliemans, R.V.A., 1984. A theoretical model for core-annular flow of a very viscous oil core and a water annulus through a horizontal pipe. Int. J. Multiphase Flow 10, 41–60, 1.
Ooms, G., Vuik, C., Poesio, P., 2007. Core-annular flow through a horizontal pipe: hydrodynamic counterbalancing of buoyancy force on core. Phys. Fluids 19, 092103, 9.
Ooms, G., Pourquié, M.J.B.M., Poesio, P., 2012. Numerical study of eccentric core-annular flow. Int. J. Multiphase Flow 42, 74–79.
Ooms, G., Pourquié, M.J.B.M., Beerens, J.C., 2013. On the levitation force in horizontal core-annular flow with a large viscosity ratio and small density ratio. Phys. Fluids 25, 032102, 3.
Roccon, A., Zonta, F., Soldati, A., 2019. Turbulent drag reduction by compliant lubricating layer. J. Fluid Mech. 863 (R1), 1-11.
Roccon, A., Zonta, F., Soldati, A., 2021. Energy balance in lubricated drag reduced turbulent channel flow. J. Fluid Mech. 911 (A37), 1–36.
Shi, J., Gourma, M., Yeung, H., 2017a. CFD simulation of horizontal oil-water flow with matched density and medium viscosity ratio in different flow regimes. J. Petroleum Sci. Eng. 151, 373–383.
Shi, J., Lao, L., Yeung, H., 2017b. Water-lubricated transport of high-viscosity oil in horizontal pipes: the water holdup and pressure gradient. Int. J. Multiphase Flow 96, 70–85.
Song, B., Plana, C., Lopez, J.M., Avila, M., 2019. Phase-field simulation of core-annular pipe flow. Int. J. Multiphase Flow 117, 14–24.
Van Duin, E., Henkes, R.A.W.M., Ooms, G., 2019. Influence of oil viscosity on oil-water core-annular flow through a horizontal pipe. Petroleum 5 (2), 199–205.
Yamamoto, T., Okano, Y., Dost, S., 2017. Validation of the S-CLSVOF method with the density-scaled balanced continuum surface force model in multiphase systems coupled with thermocapillary flows. Int. J. Numer. Methods Fluids 83 (3), 223–244.